Sr$_2$IrO$_4$/Sr$_3$Ir$_2$O$_7$ superlattice for a model two-dimensional quantum Heisenberg antiferromagnet

Hoon Kim [1,2,*] Joel Bertinshaw,[3,*] J. Porras,[3] B. Keimer,[3] Jungho Kim [4] J.-W. Kim [4] Jimin Kim [1,2]
Jonghwan Kim,[2,5] Gahee Noh,[5] Gi-Yeop Kim,[5] Si-Young Choi,[5] and B. J. Kim[1,2,†]

[1]*Department of Physics, Pohang University of Science and Technology, Pohang 790-784, Republic of Korea*
[2]*Center for Artificial Low Dimensional Electronic Systems, Institute for Basic Science (IBS),*
77 Cheongam-Ro, Pohang 37673, South Korea
[3]*Max Planck Institute for Solid State Research, Heisenbergstraße 1, D-70569 Stuttgart, Germany*
[4]*Advanced Photon Source, Argonne National Laboratory 9700 Cass Ave, Lemont, Illinois 60439, USA*
[5]*Department of Materials Science and Engineering, Pohang University of Science and Technology, Pohang 37673, South Korea*

Spin-orbit entangled pseudospins hold promise for a wide array of exotic magnetism ranging from a Heisenberg antiferromagnet to a Kitaev spin liquid depending on the lattice and bonding geometry, but many of the host materials suffer from lattice distortions and deviate from idealized models in part due to inherent strong pseudospin-lattice coupling. Here, we report on the synthesis of a magnetic superlattice comprising the single ($n = 1$) and the double ($n = 2$) layer members of the Ruddlesden-Popper series iridates Sr$_{n+1}$Ir$_n$O$_{3n+1}$ alternating along the c axis, and provide a comprehensive study of its lattice and magnetic structures using scanning transmission electron microscopy, resonant elastic and inelastic x-ray scattering, third harmonic generation measurements, and Raman spectroscopy. The superlattice is free of the structural distortions reported for the parent phases and has a higher point group symmetry, while preserving the magnetic orders and pseudospin dynamics inherited from the parent phases, featuring two magnetic transitions with two symmetry-distinct orders. We infer weaker pseudospin-lattice coupling from the analysis of Raman spectra and attribute it to frustrated magnetic-elastic couplings. Thus, the superlattice expresses a near ideal network of effective spin-one-half moments on a square lattice.

DOI: 10.1103/PhysRevResearch.4.013229

I. INTRODUCTION

The physics of an $S = 1/2$ antiferromagnet (AFM) on a two-dimensional (2D) square lattice has a long history of research as it is widely believed to hold the key for the mechanism of high-temperature superconductivity in copper oxide compounds [1–5]. However, it is rarely realized outside of Cu-based compounds and, as a result, its generic features are difficult to isolate from material specifics. Ruddlesden-Popper (RP) series iridates Sr$_{n+1}$Ir$_n$O$_{3n+1}$, have recently emerged as a new material platform to study the same physics with spin-orbit entangled $J_{\text{eff}} = 1/2$ pseudospins replacing the $S = 1/2$ moments in the cuprates [6–10]. Indeed, the single layer Sr$_2$IrO$_4$ has reproduced much of the cuprate phenomenology: a pseudogapped metal [11–13] and a nodal metal with a d-wave symmetric gap indicative of possible unconventional superconductivity [14,15] emerge upon electron doping from the parent phase that is approximately a Heisenberg AFM [16,17]. Further, experiments indicate the existence of various symmetry-breaking orders: polarized neutron

diffraction [18] detects time-reversal symmetry breaking above the Néel temperature (T_N), magnetic torque [19] and second harmonic generation [20,21] measurements indicate loss of C_4 rotation symmetry, and resonant x-ray diffraction [22] observes splitting of a magnetic Bragg peak, suggesting formation of a nearly commensurate density wave.

However, iridates are different from the cuprates in several aspects, and to what extent they are relevant to the essential physics is an open important issue. First, the dominant orbital character of the pseudospins leading to strong pseudospin-lattice coupling (PLC) [23–25], which accounts largely for the spin-wave gap, questions the validity of spin-only models. Second, structural distortions of kinds not found in cuprates [26–28] add complexity to theory models by allowing additional interactions. For example, the staggered tetragonal distortion of IrO$_6$ octahedra in Sr$_2$IrO$_4$, breaking the vertical glide planes and thus lowering the space group from $I4_1/acd$ to $I4_1/a$ [26,27], leads to additional pseudospin exchange interactions, which provide a mechanism for locking of pseudospin canting angles and the octahedral rotation [29]. In the bilayer compound Sr$_3$Ir$_2$O$_7$, the monoclinic distortion, lowering the space group from orthorhombic $Bbca$ to monoclinic $C2/c$ [28] results in bending of otherwise straight Ir–O–Ir c-axis bonds. This in turn leads to canting of the AFM moments aligned along the c axis, manifesting as small but clearly measurable net in-plane ferromagnetic moments [30,31]. Such distortions lead to deviation from the ideal cubic-symmetric $J_{\text{eff}} = 1/2$ states on rectilinear superexchange pathways, which are assumed in theory models that
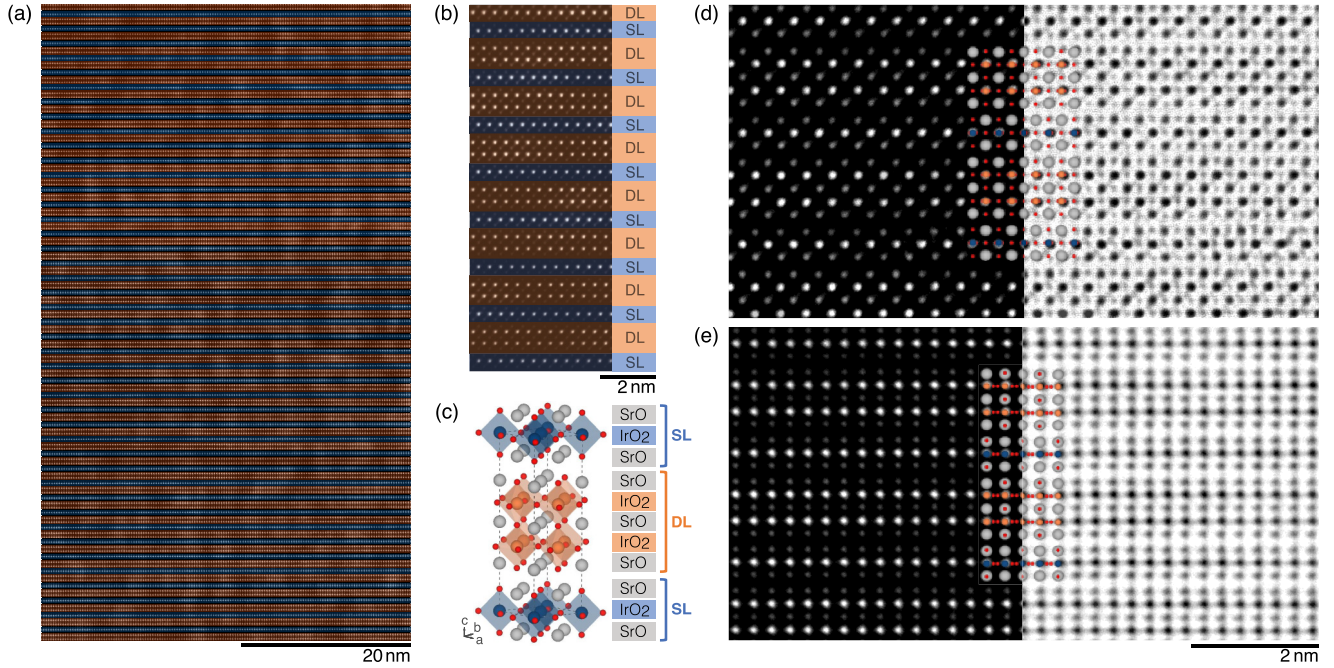

FIG. 1. Stacking pattern of the superlattice as imaged by STEM. (a) Wide field-of-view STEM image along [100] projection. The alternation between single layers (blue) and double layers (orange) is well maintained over the entire field of view. (b) Magnified HAADF-STEM image with single layer (blue) and double layer (orange) indicated. (c) A structural model for the superlattice. The single layer and double layer are shifted by a half unit cell on the SrO planes. IrO_6 octahedra are rotated about the c axis as in the parent compounds. (d) [110]- and (e) [100]-projected HAADF (left)- and ABF (right)-STEM images overlaid with the atom positions (Sr, grey; Ir, blue, orange; O, red) from the model.

predict, for example, realization of a Kitaev spin liquid in a honeycomb lattice [8,32].

Here, we report on the synthesis of a $Sr_2IrO_4/Sr_3Ir_2O_7$ superlattice and provide a comprehensive study of its lattice and magnetic structures. The lattice structure is investigated by scanning transmission electron microscopy (STEM), resonant x-ray diffraction (RXD), and rotational anisotropy third harmonic generation measurements (RA-THG), and the magnetic structure by magnetometry, RXD, resonant inelastic x-ray scattering (RIXS), and Raman scattering. The superlattice is free of structural distortions reported for the parent phases while leaving their magnetic structures intact. The superlattice features two magnetic transitions with two different orders: canted *ab*-plane AFM and *c*-axis collinear AFM inherited from Sr_2IrO_4 and $Sr_3Ir_2O_7$, respectively. Their contrasting pseudospin dynamics, of Heisenberg and Ising types, also remain unchanged within our experimental resolutions. However, *ab*-plane magnetic anisotropy of the Heisenberg pseudospins is significantly reduced, indicating weaker PLC, possibly due to the Ising pseudospins aligned along the *c* axis resisting the orthorhombic distortions. Our result shows that two distinct types of quasi-2D magnetism can be compounded in a superlattice to realize a pseudospin system closer to an ideal model.

II. METHODS

STEM measurements were conducted using JE-MARM200F, JEOL at 200 kV with fifth-order probe-corrector (ASCOR, CEOS GmbH, Germany). The specimens were prepared by a dual-beam focused ion beam

with Ga ion beams of $1 \sim 5$ kV (Nanolab G3 CX, FEI) and further milled by Ar ion beams of 100 meV (PIPS II, Gatan) to minimize the surface damage. RXD and RIXS measurements were carried out at Beamline 6-ID-B and Beamline 27-ID, respectively, at the Advanced Photon Source, Argonne National Laboratory. For RA-THG measurements, we adapted the scheme reported in Ref. [37] by replacing the phase mask by a pair of wedge prisms to accommodate a wider wavelength range of incident light (from 800 nm to 1200 nm). The incident 1200-nm light was provided by an optical parametric amplifier (Orpheus-F, Light Conversion) powered by a femtosecond laser of 100 kHz repetition rate (Pharos, Light Conversion). The laser fluence is kept below $2 \, mJ/cm^2$ and the beam spot size is $\sim 40 \, \mu m$ full width at half maximum. Raman spectroscopy is measured with a 633-nm He-Ne laser, which a beam of 0.8 mW is focused on $\sim 2 \, \mu m$.

III. LATTICE STRUCTURE

The superlattice has the nominal chemical composition $Sr_5Ir_3O_{11}$ and can be regarded as a $n = 1.5$ member of the RP series. Although this phase is not quite thermodynamically stable, it forms transiently during a flux growth before either the $n = 1$ or $n = 2$ phase eventually stabilizes, depending on the starting composition of Sr_2CO_3 and IrO_2 molten in $SrCl_2$ flux and dwelling temperature. Thermal quenching at high temperature leads to intergrowth of both phases, and a highly ordered superlattice can be found by a careful control of the heating sequence. The resulting crystals typically have a few microns thickness, thicker than layer-by-layer grown
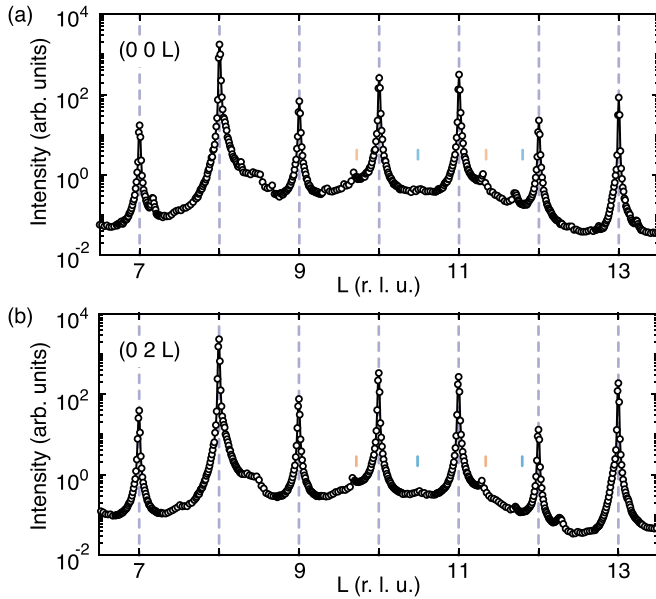
FIG. 2. RXD on the superlattice at the Ir L_3-edge. Sharp (a) (0 0 L) and (b) (0 2 L) charge reflections are centered at integer-L values (dashed lines), indicating the superlattice is well ordered across the bulk of the sample. Minor impurity peaks that match Sr$_2$IrO$_4$ and Sr$_3$Ir$_2$O$_7$ are marked by cyan and orange sticks, respectively. Miller indices are in the orthorhombic notation; i.e., reciprocal lattice vectors corresponding to the unit cell shown in Fig. 1(c).

FIG. 3. RA-THG patterns of the superlattice (open circles) taken under (a) *PP*, (b) *PS*, (c) *SP*, (d) *SS* geometries. Incident 1200 nm light was used at room temperature. The third harmonic 400 nm light was collected as a function of azimuth angle while the scattering plane rotates about *c* axis [36,37]. The THG signals are normalized by the *PP* trace, overlaid with the best fits to bulk electric dipole induced THG tensor of 4/*mmm* point group (navy lines).

thin films but thinner than typical bulk crystals. As the conventional structure refinement is limited by the small sample volume, we rely on STEM and RXD to verify the superlattice formation.

Figure 1(a) shows a wide field-of-view STEM image along [100] projection showing the stacking of single (SL) and double-layer (DL) units alternating over >40 unit cells. The stacking sequence is indicated in Fig. 1(b) and the unit cell is depicted in Fig. 1(c), which is modeled from the known structures of Sr$_2$IrO$_4$ (Ref. [33]) and Sr$_3$Ir$_2$O$_7$ (Ref. [34]). Figures 1(d) and 1(e) show representative high-angle annular dark field (HAADF) and annular bright field (ABF) images along [110] projection and [100] projection, respectively. The images are overlaid with the atomic positions based on the unit cell in Fig. 1(c). In the [100] projection, the staggered rotation of IrO$_6$ octahedra about the *c* axis as in the parent compounds is seen as diffuse rods (see also Figs. 8 and 9 in Appendix A). Overall, our data is in good agreement with the model.

The superlattice formation is confirmed to represent the bulk of the sample via RXD conducted at the Ir L_3-edge. Figures 2(a) and 2(b) plot scans along (0 0 L) and (0 2 L), respectively, which show reflections centered at integer-L values with $\sim$0.01 Å widths. Impurity peaks of intensities of the order of $\lesssim$1 % of the main peaks are observed, which match the *c*-axis lattice parameters of either Sr$_2$IrO$_4$ or Sr$_3$Ir$_2$O$_7$. The sharp reflections and negligible impurity peaks indicate that the superlattice structure remains well correlated at a macroscopic level. Whereas the in-plane lattice parameters ($\approx$5.502 Å) match those of the parent systems, the *c* axis is unique with a length of 16.93 Å. According to the study by Harlow *et al.* [35], however, diffraction patterns from a
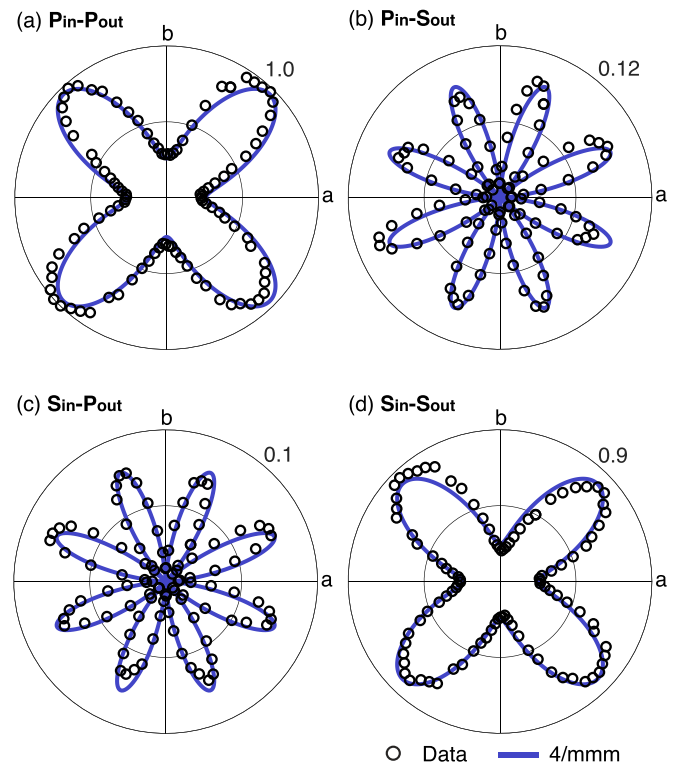
randomly-stacked intergrowth of $n = 1$ and $n = 2$ phases can misleadingly appear similar to those of an ordered phase. Such possibility is ruled out in our sample by selectively measuring the periodicity of DL, by exploiting the fact that only DLs are magnetically ordered in the temperature range between $T = 220$ K and 280 K (to be discussed in Sec. III).

Next, we further refine the structure using RA-THG, a nonlinear optical process highly sensitive to the bulk crystal symmetry through nonlinear susceptibility tensors [36–38]. This technique has been used for Sr$_2$IrO$_4$ and Sr$_3$Ir$_2$O$_7$ to detect subtle structure distortions [21,27,28]. Figure 3 shows the azimuth-angle dependence of the third harmonic signals as the scattering plane is rotated about the *c* axis, for the four different polarization configurations of the incident and reflected light, which can be either parallel (*P*) or perpendicular (*S*) to the scattering plane. The patterns are symmetric with respect to mirror reflections $a \rightarrow -a$ and $b \rightarrow -b$, and fourfold rotations about the *c* axis. The combination of both symmetries leads to eightfold symmetric patterns for the *PS* and *SP*. To confirm, the patterns are overlaid with the best fit to electric-dipole induced THG tensor for 4/*mmm* (navy), whose expression is given in Appendix B. We find an excellent agreement and conclude that the superlattice has a higher point group symmetry than Sr$_2$IrO$_4$ (Ref. [27]) and Sr$_3$Ir$_2$O$_7$ (Ref. [28]), in both of which the patterns manifestly lack the mirror symmetries.
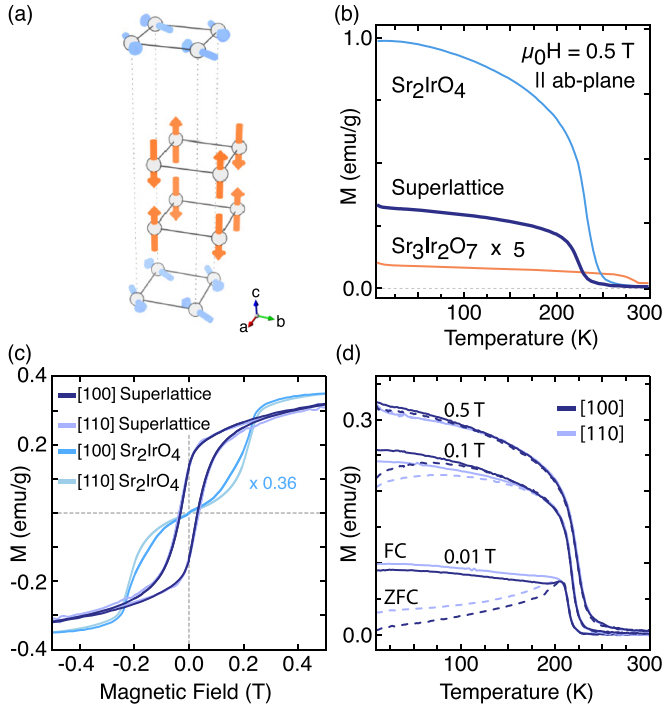
FIG. 4. Magnetometry of the superlattice. (a) The superlattice magnetic order consistent with our data. (b) Field-cooled M-T curves of the superlattice (navy), Sr_2IrO_4 (cyan) and $Sr_3Ir_2O_7$ (orange). (c) M-H hysteresis at 5 K comparing the superlattice (navy) and the bulk Sr_2IrO_4 (cyan). For a direct comparison, Sr_2IrO_4 curves are multiplied by the mass proportion (≈ 0.36) of SL in the superlattice. (d) M-T curves measured with fields applied along [100] and [110].

IV. MAGNETIC STRUCTURE

Having established the lattice structure of the superlattice, we now turn to its magnetic structure. In short, the magnetic structure remains almost unchanged from the parent systems: SL has an *ab*-plane canted AFM structure while DL has a *c*-axis collinear AFM structure, as shown in Fig. 4(a). The net ferromagnetic response to the dc field with the saturation moment close to one-third of that of Sr_2IrO_4 [Figs. 4(b) and 4(c)] suggests that the SL (which makes up one-third of the superlattice in terms of the number of Ir ions) has in-plane canted AFM structure, while DL has *c*-axis collinear AFM structure. We note that the AFM ordering in $Sr_3Ir_2O_7$ is visible as a small jump in the magnetization due to its slight monoclinicity $\beta \sim 90.05°$ (and thereby canting of the moments [28,30]), but no such anomaly indicative of DL magnetic ordering is seen in our tetragonal superlattice [Fig. 4(b)]. Unlike in Sr_2IrO_4, we observe a ferromagnetic hysteresis loop in the M-H curve shown in Fig. 4(c), which implies ferromagnetic staking of SL net moments. Based on our M-H and M-T curves [Figs. 4(c) and 4(d)] measured for fields along [100] and [110] directions, we are not able to identify the magnetic easy axis in the *ab* plane, which in Sr_2IrO_4 is clearly along the *a* axis [23,24]. This signifies reduced magnetic anisotropy, which will be discussed in more detail later on.

We confirm the magnetic structure shown in Fig. 4(a) using RXD. As in the case of Sr_2IrO_4 and $Sr_3Ir_2O_7$, magnetic reflections are found along (1 0 L) [Fig. 5(a)], but at every
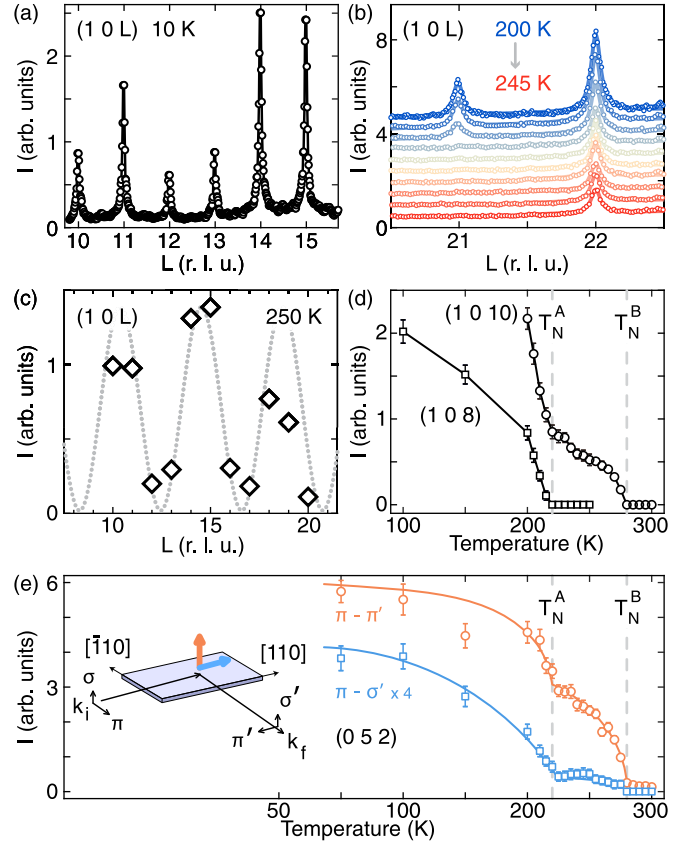

FIG. 5. Magnetic RXD study on the superlattice. (a) Magnetic (1 0 L) reflections appear at every integer L value, contributed by signals from both SL and DL. (b) (1 0 L) scans measured at every 5 K upon heating from 200 K to 245 K. (1 0 21) reflection dominated by SL disappears around $T = 220$ K. (c) At 250 K, the intensity modulation along (1 0 L) coincides with DL structure factor squared (dotted line), indicating that the magnetic intensities are dominated by DL. (d) Temperature dependence of (1 0 8) and (1 0 10) reveal two magnetic transitions at $T_N^A = 220$ K and $T_N^B = 280$ K. (e) Polarization analysis to separate AFM signals from in-plane (blue) and out-of-plane (orange) moments.

integer L, which has contributions from both SL and DL. However, they can be separated by exploiting the DL structure factor. The ratio of the Ir–O–Ir bond length along the *c*-axis to *c*-lattice parameter returns an oscillation period of $\sim$4.15. For example, the DL contribution nearly vanishes for (1 0 8) and (1 0 21). Indeed, L scans shown in Fig. 5(b) shows that (1 0 21) peak disappears around $T = 220$ K as temperature increases while (1 0 22) peak is present up to $T = 250$ K. At this temperature, the intensity modulation well agrees with the DL structure factor squared [Fig. 5(c)], implying that the peaks are due to reflections from DL only. This is unambiguous evidence for coherent superlattice formation over the probing depth of x-ray (290 nm $\sim 3.1 \,\mu$m as calculated in Ref. [39]). The SL transition temperature is measured to be $T_N^A = 220$ K from the temperature dependence of (1 0 8) peak shown in Fig. 5(d). At (1 0 10), two transitions are seen, the higher temperature one at $T_N^B = 280$ K being the transition in DL.
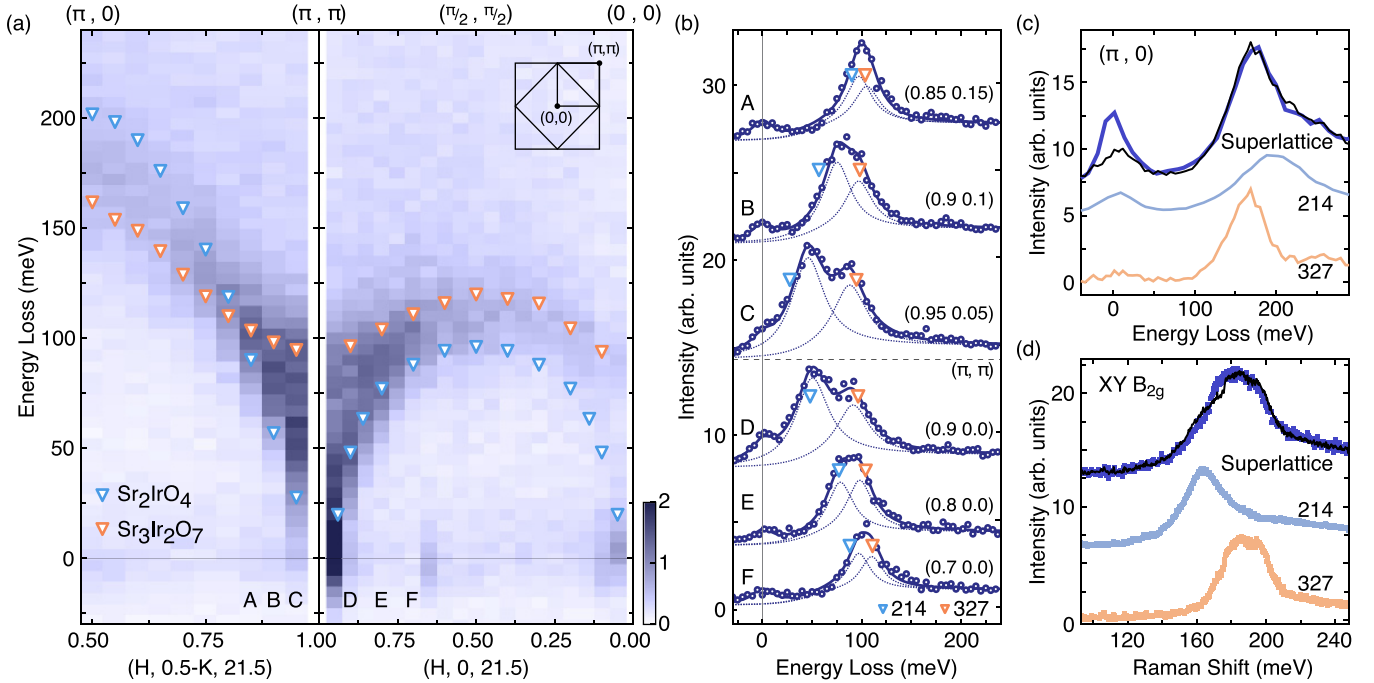
FIG. 6. Magnetic excitations in the superlattice. (a) RIXS map measured at $T = 10$ K along high-symmetry directions indicate that the SL and DL modes follow the dispersions of the parent systems (plotted with markers). (b) Spectra at select **q** points. The fitted peaks (solid lines) are compared with those of the parent systems (markers). (c) The superlattice spectrum at the zone corner $(\pi, 0)$ (navy line) is well reproduced by a linear sum of Sr$_2$IrO$_4$ and Sr$_3$Ir$_2$O$_7$ spectra (black line). (d) The two-magnon Raman spectrum (navy dots), measured in the B_{2g} channel at $T = 15$ K, is also well approximated by summing the Sr$_2$IrO$_4$ and Sr$_3$Ir$_2$O$_7$ spectral intensities (black line).

Additional measurements were conducted using polarization analysis to separate the *ab*-plane and *c*-axis components of the antiferromagnetic moments. By studying the magnetic (0 5 2) reflection in a horizontal scattering geometry [Fig. 5(e)], the π-σ' channel mostly detects in-plane moments, whereas π-π' is sensitive to out-of-plane moments. The temperature dependence of the integrated intensities in the two channels, shown in Fig. 5(e), reveals that the out-of-plane (in-plane) magnetic signal arises below $T_N^B = 280$ K ($T_N^A = 220$ K), thereby located at DL (SL), consistent with the magnetic structure in Fig. 4(a).

V. PSEUDOSPIN DYNAMICS

Having established the static magnetic structure, we now turn to the pseudospin dynamics. Figure 6(a) plots the pseudospin excitation spectrum along high symmetry directions. Select **q** points are plotted in Fig. 6(b). The spectra are fitted with two peaks and their energy positions are compared with the spin-wave dispersions for the parent systems. Overall, the spectra are well described as having two peaks corresponding to spin waves in SL and DL. It is known that Sr$_2$IrO$_4$ is almost gapless at the magnetic zone center reflecting the quasicontinuous symmetry in the *ab*-plane [16], whereas Sr$_3$Ir$_2$O$_7$ has an exceptionally large gap of ≈ 90 meV (Ref. [40]). Except in the immediate vicinity of the magnetic zone center, we find good agreement with the parent systems. In particular, the spectra at the zone corner $(\pi, 0)$ is well reproduced by a linear sum of the spectra of Sr$_2$IrO$_4$ and Sr$_3$Ir$_2$O$_7$ at the same momenta, as shown in Fig. 6(c). Further, the two-magnon

spectrum measured by Raman scattering [Fig. 6(d)], which is dominated by zone-boundary modes, is in perfect agreement with a linear sum of those in Sr$_2$IrO$_4$ and Sr$_3$Ir$_2$O$_7$. Together, these data indicate that the nearest-neighbor spin exchange couplings remain unaltered with respect to the parent systems.

It is perhaps not surprising that there is no significant change in the pseudospin dynamics across the majority of the Brillouin zone for both SL and DL, considering that these are quasi-2D systems and only the stacking sequence is altered. However, it is rather unusual that the two magnetic subsystems behave almost independently of each other. In particular, magnetic ordering in DL occurs across SL that remains paramagnetic down to T_N^A. That no other static order exists in SL above T_N^A is confirmed from its almost identical RIXS spectra measured across T_N^A (Fig. 11 in Appendix D). Our representation analysis (Appendix E) shows that the SL and the DL magnetic orders belong to different irreducible representations, which guarantees that they are not coupled in the linear order (this, however, does not rule out interactions between SL and DL). Further, we note that both T_N^A and T_N^B are reduced only by few degrees from their bulk counterparts, which confirms that interlayer couplings play a minor role in the critical phenomena [8,41,42].

While the magnetic properties of the superlattice are mostly inherited from the parent Sr$_2$IrO$_4$ and Sr$_3$Ir$_2$O$_7$, some differences are also found. Unlike in the case of Sr$_2$IrO$_4$, the in-plane magnetic anistropy of SL is hardly visible in the magnetometry data [Fig. 4(c)]. In Sr$_2$IrO$_4$, the magnetic anisotropy is known to arise mostly from PLC [23,24], stabilizing the magnetic ordering along the *a* or *b* axis. The PLC
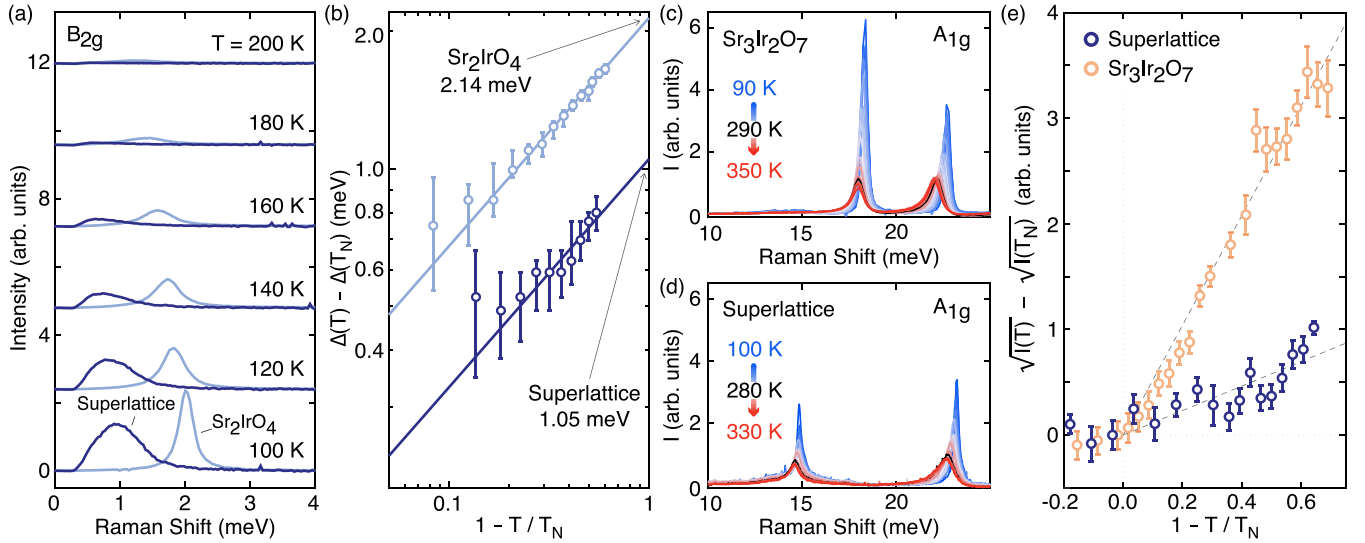
FIG. 7. Pseudospin-lattice coupling estimated by Raman spectroscopy. (a) The magnetic mode at the zone center is observed in B_{2g} scattering geometry (superlattice, navy; Sr_2IrO_4, blue gray). (b) The temperature-dependent component of the spin-wave gap $\Delta(T)$ extracted from Raman spectra in (a). The trend of the superlattice and Sr_2IrO_4 share the same functional form $A\sqrt{1 - T/T_N} + B$, where A is the offset in the log-log plot and proportional to the strength of PLC. Temperature dependence of A_{1g} phonons in (c) $Sr_3Ir_2O_7$ and (d) the superlattice. (e) Integrated intensity of the lower energy A_{1g} phonon. The spin-dependent component scales with the ordered moment squared M_{AFM}^2, and dashed lines are fits to functional form of $1 - (T/T_N)$, whose slopes are proportional to the PLC strength Λ. All Raman spectra are corrected for laser heating and Bose factors.

dominates over the nearest-neighbor pseudospin exchange anisotropies favoring alignment along the bond directions (i.e., along [110]), and also accounts for a dominant part of the in-plane magnon gap [24]. To compare the strength of PLC, we analyze the temperature dependence of Raman spectra in the B_{2g} symmetry channel, which measures the magnon gap at the zone center [see Fig. 7(a)]. It is seen in Fig. 7(b) that the magnon gap of both Sr_2IrO_4 and the superlattice follow the same mean-field-like functional form of $A\sqrt{1 - T/T_N} + B$, where the temperature-independent constant B arises from anisotropic magnetic interactions, and A measures the strength of PLC that scales with the size of the ordered moment [23–25]. From the intercept at $T = 0$ in the log-log plot shown in Fig. 7(b), we find that the PLC is drastically reduced by a factor of 2. The reduced PLC in SL can be understood in terms of the structural rigidity provided by DL resisting orthorhombic distortions, which would be energetically unfavorable for the c-axis collinear AFM structure.

An indication of suppressed PLC can also be found from a phonon mode strongly coupled to the AFM order in DL. In $Sr_3Ir_2O_7$, a recent ultrafast optical spectroscopy study has shown that strong PLC manifests as an abrupt large enhancement across T_N of the amplitude of the coherent oscillation of the impulsive 4.4 THz (≈ 18 meV) A_{1g} phonon mode [25]. The intensity follows the phenomenological relation $\sqrt{I(T)} \propto Z - (\Lambda/4\mu_B^2)M_{AFM}^2$, where Λ and Z are the PLC strength and temperature-independent spectral weight, respectively [43]. The strength of PLC in $Sr_3Ir_2O_7$ is estimated to be two orders of magnitude stronger than in cubic perovskite manganites with strong spin-lattice couplings [44]. Since the oscillation amplitude is linearly dependent on Raman tensor $\partial\alpha/\partial Q$ [45], where α is the polarizability and Q is the normal coordinate

of the phonon mode, the enhancement should be also visible in Raman spectra. Indeed, we observe a strong enhancement upon cooling of the 18 meV A_{1g} mode intensity as shown in Fig. 7(c). However, the corresponding mode in the superlattice at ≈ 15 meV shows only a modest increase comparable to that of the 23 meV mode [Fig. 7(e)]. Taken as a whole, the absence of discernible anisotropy in the magnetization data, the reduced magnon gap, and the insensitivity of the A_{1g} mode to the magnetic order all consistently point to significant reduction of PLC in the superlattice.

VI. SUMMARY

Recent advances in the control and understanding of 2D materials has recently expanded into the research of magnetism in the extreme quantum 2D limit and in artificial heterostructures. In this paper, we have demonstrated successful growth of a $Sr_2IrO_4/Sr_3Ir_2O_7$ magnetic superlattice, whose constituent bulk phases exhibit quantum magnetism in the limit of strong spin-orbit coupling. While intergrowth of different phases in a RP series is frequently found, a natural formation of an ordered superlattice is extremely rare. The superlattice has a lattice symmetry higher than those of the bulk phases and realizes an undistorted square lattice geometry. Thus, the superlattice offers a unique opportunity to study the pseudospin physics in an ideal setting.

The superlattice preserves the bulk magnetic orders and interleaves *ab*-plane canted AFM and *c*-axis collinear AFM alternately stacked along the *c* axis. The two mutually orthogonal orders, however, behave independently of each order, reflecting weak interlayer couplings expected for quasi-2D systems. In particular, there is a temperature range where only one magnetic subsystem develops an order across the other

that remains paramagnetic. Further, the pseudospin dynamics remains unchanged from the parent systems for the most part of the Brillouin zone.

Instead, the incompatible nature of the magnetic orders manifests as a strong suppression of the PLC, which is expected to be generally strong for iridates. The reduced PLC in SL is inferred from the smaller zone-center magnon gap, which in Sr$_2$IrO$_4$ is largely accounted for by the PLC through a pseudo-Jahn-Teller effect that results in an orthorhombic distortion as the *ab*-plane magnetic order breaks the tetragonal symmetry of the lattice. This effect, however, is counteracted in the superlattice by DL. The magnetic order in DL is collinear along the straight *c*-axis bond, which in Sr$_3$Ir$_2$O$_7$ is bent due to a slight monoclinicity.

The origin of the distortions in the parent compounds and their absence in the superlattice is a subject of future research. To the best of our knowledge, the breaking of glide symmetries as seen in Sr$_2$IrO$_4$, attributed to staggered tetragonal distortions, is not found in any other transition-metal compounds of the RP type, which suggests that the distortion is not due to an instability of the lattice but rather its interactions with pseudospins whose magnetic moment size strongly depends on lattice distortions. Similarly, it remains to be understood if PLC plays any role in stabilizing the monoclinic structure in Sr$_3$Ir$_2$O$_7$. At any rate, many iridates in bulk form exhibit lattice distortions of some sort and deviate from idealized models, and in this regard the superlattice stands out as a realization of pseudospin one-half physics on an undistorted square lattice.

The persistent magnetic orders in the superlattice also allows investigation of their evolution upon carrier doping. It is known that Sr$_3$Ir$_2$O$_7$ is on the verge of a metal-insulator transition, and therefore it may well be that DL turns into a Fermi liquid metal while SL remains a correlated fluid, a situation akin to the case of electron-doped Sr$_2$IrO$_4$ via surface alkali metal dosing, where Fermi arcs and a *d*-wave gap are observed, which possibly involve screening effects from the surface metallic layer. Our results presented here provide a solid foundation for these future investigations.

APPENDIX A: STEM ANALYSIS ON THE PARENT COMPOUNDS

To aid the structure analysis of the Sr$_2$IrO$_4$/Sr$_3$Ir$_2$O$_7$ superlattice, we performed STEM analysis on Sr$_2$IrO$_4$ [Fig. 8(a)] and Sr$_3$Ir$_2$O$_7$ [Fig. 9(a)] single crystals which serve as reference. Figures 8(b) and 9(b) show a representative HAADF-STEM image and ABF-STEM images of Sr$_2$IrO$_4$ and Sr$_3$Ir$_2$O$_7$, respectively, which reveal the high quality of crystallization of the stacking pattern. Figures 8(c) and 8(d) are high magnifications HAADF- and ABF-STEM images of Sr$_2$IrO$_4$ in the [110] and [100] projections, respectively,

FIG. 8. Crystal structure of Sr$_2$IrO$_4$. (a) Crystal structure along [110] projection. Each layer is shifted by a half unit cell on the SrO planes. (b) HAADF-STEM image (left) and ABF-STEM image (right) in the [110] projection show the highly ordered stacking pattern. (c) [110]- and (d) [100]-projected HAADF (left)- and ABF (right)-STEM images overlaid with the atom positions (Sr, grey; Ir, blue; O, red).
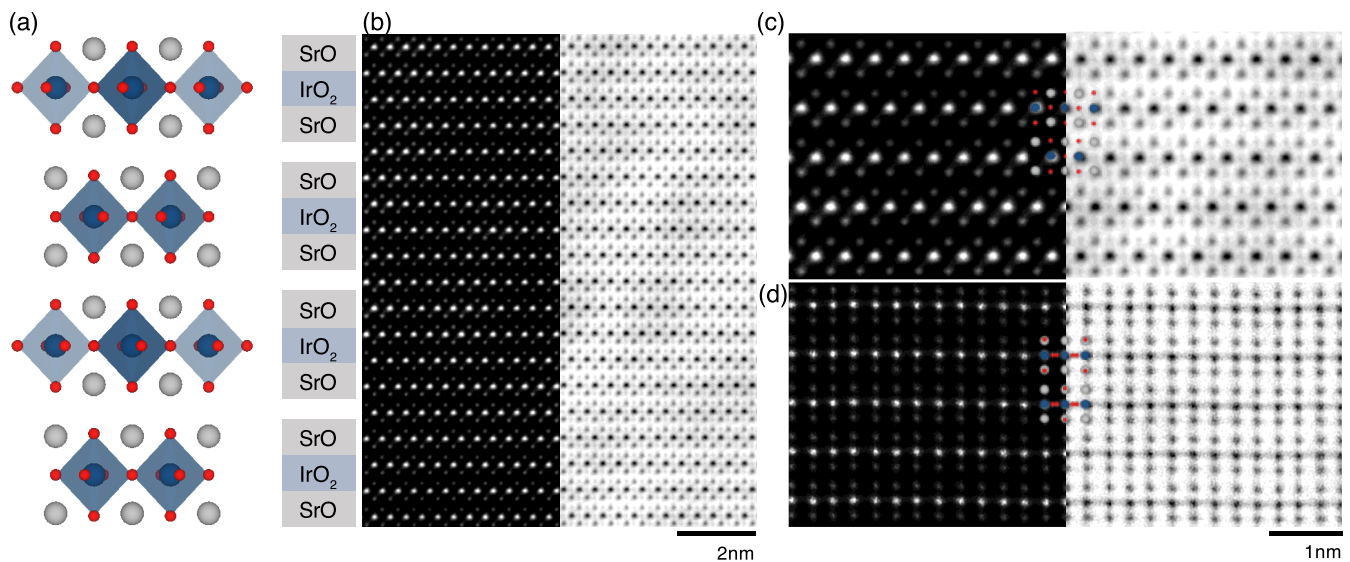
FIG. 9. Crystal structure of $Sr_3Ir_2O_7$. (a) Crystal structure along [110] projection. Each layer is shifted by a half unit cell on the SrO planes. (b) HAADF-STEM image (left) and ABF-STEM image (right) in the [110] projection show the highly ordered stacking pattern. (c) [110]- and (d) [100]-projected HAADF (left)- and ABF (right)-STEM images overlaid with the atom positions (Sr, grey; Ir, orange; O, red).
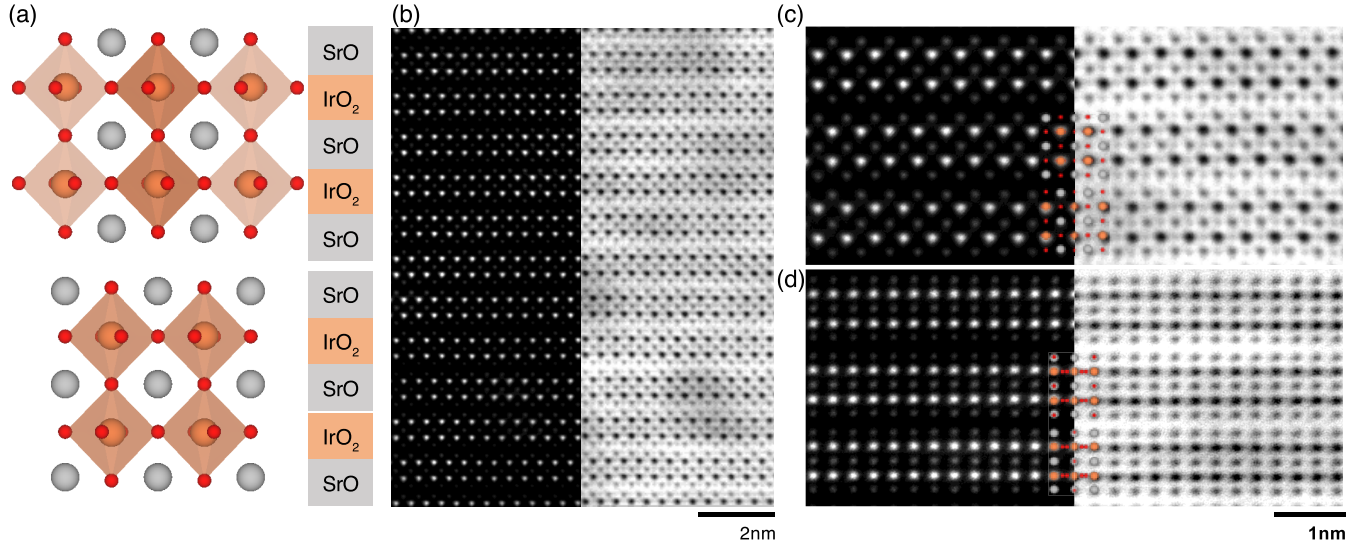
which show that the STEM images are consistent with the crystal structure reported in Ref. [33]. Likewise, Figs. 9(c) and 9(d) are high magnification HAADF- and ABF-STEM images of $Sr_3Ir_2O_7$ in the [110] and [100] projections, respectively, which are consistent with the crystal structure reported in Ref. [30]. In both structures, IrO_6 octahedra rotations about the c axis are visible in the [100]-projected ABF-STEM images as diffuse rods [Figs. 8(d) and 9(d)], in contrast to pointlike structures seen in the [110]-projected images [Figs. 8(c) and 9(c)].

The simulation for the superlattice is based on a model that combines the structures of Sr_2IrO_4 and $Sr_3Ir_2O_7$ for the SL and the DL units, respectively. Assuming the same octahedra rotation pattern as in the parent compounds, the relative sense of rotation between two reference octahedra in SL and

DL uniquely determine the structure, provided that the unit cell comprises one SL and one DL. Although the octahedra rotations are clearly visible in the superlattice [Fig. 1(e)], the sense of rotation could not be determined from our data.

The simulation suggests $P\bar{4}b2$ space group (No. 117), whose point group is $\bar{4}m2$. A main difference from the $4/mmm$ point group is the absence of inversion symmetry, which is due to the fact that the superlattice contains three IrO_6 layers with different octahedral rotations. An inversion symmetric structure model can be made with a larger unit cell. However, our main results do not rely on the details of such a possible superstructure formed by octahedral rotations, and thus we work with the smallest possible unit cell consistent with all our data.

APPENDIX B: THIRD HARMONIC GENERATION TENSORS

We obtain the general form of the bulk electric dipole induced THG tensor for the $4/mmm$ (and $\bar{4}m2$) point group by starting from the most general form of a fourth-rank Cartesian tensor and requiring it to be invariant under all the symmetry operations contained in the group as

$$\chi^{\text{ED}}_{ijkl} = \begin{pmatrix} \begin{pmatrix} xxxx & 0 & 0 \\ 0 & xxyy & 0 \\ 0 & 0 & xxzz \end{pmatrix} & \begin{pmatrix} 0 & xxyy & 0 \\ xxyy & 0 & 0 \\ 0 & 0 & 0 \end{pmatrix} & \begin{pmatrix} 0 & 0 & xxzz \\ 0 & 0 & 0 \\ xxzz & 0 & 0 \end{pmatrix} \\ \begin{pmatrix} 0 & xxyy & 0 \\ xxyy & 0 & 0 \\ 0 & 0 & 0 \end{pmatrix} & \begin{pmatrix} xxyy & 0 & 0 \\ 0 & xxxx & 0 \\ 0 & 0 & xxzz \end{pmatrix} & \begin{pmatrix} 0 & 0 & 0 \\ 0 & 0 & xxzz \\ 0 & xxzz & 0 \end{pmatrix} \\ \begin{pmatrix} 0 & 0 & zxxz \\ 0 & 0 & 0 \\ zxxz & 0 & 0 \end{pmatrix} & \begin{pmatrix} 0 & 0 & 0 \\ 0 & 0 & zxxz \\ 0 & zxxz & 0 \end{pmatrix} & \begin{pmatrix} zxxz & 0 & 0 \\ 0 & zxxz & 0 \\ 0 & 0 & zzzz \end{pmatrix} \end{pmatrix}, \qquad (B1)$$

where $jkl(i)$ stands for incident(scattered) light polarizations. In our experiment, the light is incident on the sample surface normal to the c axis with the incidence angle θ and azimuth angle ψ, which is defined to be zero when the scattering plane contains the a and c axes. Then, the polarization vectors are given by

$$\vec{\epsilon}_s = (\sin\psi, -\cos\psi, 0), \quad \vec{\epsilon}_{\text{in},p} = (-\cos\theta\cos\psi, -\cos\theta\sin\psi, \sin\theta), \quad \vec{\epsilon}_{\text{out},p} = (\cos\theta\cos\psi, \cos\theta\sin\psi, \sin\theta). \quad (B2)$$
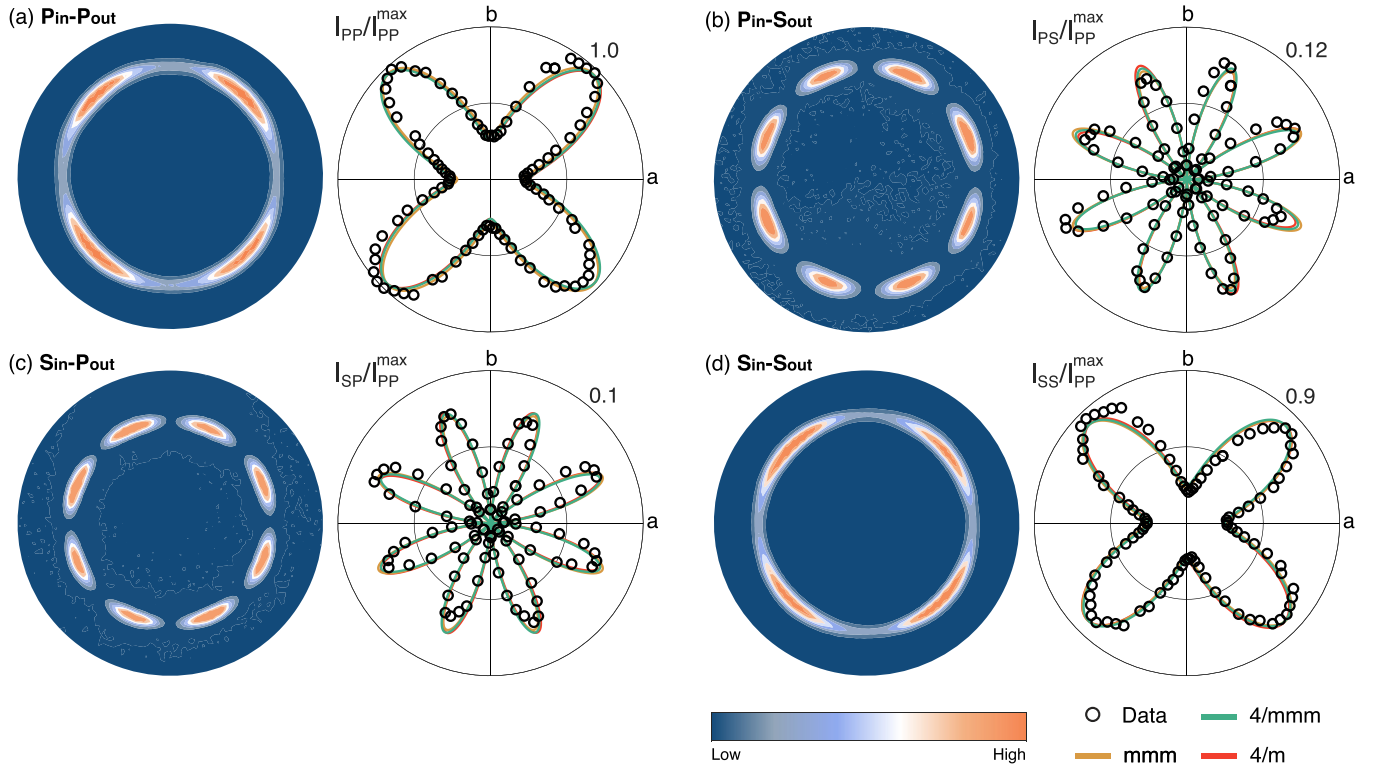
FIG. 10. Superlattice RA-THG patterns (open circles) in (a) PP, (b) PS, (c) SP, and (d) SS geometries, and their best fits to different point groups. The third harmonic light was collected on a 2D detector (left images) following the experimental schemes in Refs. [36,37]. The THG signals are extracted from the 2D images and normalized by the maximum intensity of the PP trace (right plots), overlaid with the best fits to bulk electric dipole induced THG tensors of 4/mmm (green), mmm (yellow) and 4/m (red) point groups.

Multiplying the tensor with the polarization vectors, the expressions for the THG intensity simplify as

$$I^{SS}(3\omega) \sim |A + B\cos(4\psi)|^2, \quad I^{PS}(3\omega) \sim |B\sin(4\psi)|^2, \quad I^{SP}(3\omega) \sim |B\sin(4\psi)|^2, \quad I^{PP}(3\omega) \sim |A' + B\cos(4\psi)|^2, \quad \text{(B3)}$$

where A, A', and B are adjustable parameters. The formulas are consistent with the 4/mmm point group symmetry, invariant under both mirror reflections ($\psi \rightarrow \pi - \psi$ and $\psi \rightarrow -\psi$) and C$_4$ rotation about the c-axis ($\psi \rightarrow \pi/2 + \psi$). We note that the inversion symmetry does not impose any further constraint on the tensor form and thus $\bar{4}m2$ has the same tensor form.

In the mmm point group, where x and y axes are not equivalent, the bulk electric dipole induced THG tensor is modified as

$$\chi_{ijkl}^{\text{ED}} = \begin{pmatrix} \begin{pmatrix} xxxx & 0 & 0 \\ 0 & xxyy & 0 \\ 0 & 0 & xxzz \end{pmatrix} & \begin{pmatrix} 0 & xxyy & 0 \\ xxyy & 0 & 0 \\ 0 & 0 & 0 \end{pmatrix} & \begin{pmatrix} 0 & 0 & xxzz \\ 0 & 0 & 0 \\ xxzz & 0 & 0 \end{pmatrix} \\ \begin{pmatrix} 0 & yxxy & 0 \\ yxxy & 0 & 0 \\ 0 & 0 & 0 \end{pmatrix} & \begin{pmatrix} yxxy & 0 & 0 \\ 0 & yyyy & 0 \\ 0 & 0 & yyzz \end{pmatrix} & \begin{pmatrix} 0 & 0 & 0 \\ 0 & 0 & yyzz \\ 0 & yyzz & 0 \end{pmatrix} \\ \begin{pmatrix} 0 & 0 & zxxz \\ 0 & 0 & 0 \\ zxxz & 0 & 0 \end{pmatrix} & \begin{pmatrix} 0 & 0 & 0 \\ 0 & 0 & zyyz \\ 0 & zyyz & 0 \end{pmatrix} & \begin{pmatrix} zxxz & 0 & 0 \\ 0 & zyyz & 0 \\ 0 & 0 & zzzz \end{pmatrix} \end{pmatrix}, \quad \text{(B4)}$$

leading to the following expressions for the azimuth-angle dependence of THG intensity:

$$I^{SS}(3\omega) \propto |A + B_1\cos(2\psi) + C\cos(4\psi)|^2, \quad I^{PS}(3\omega) \propto |B_2\sin(2\psi) + C'\sin(4\psi)|^2,$$

$$I^{SP}(3\omega) \propto |B_2'\sin(2\psi) + C'\sin(4\psi)|^2, \quad I^{PP}(3\omega) \propto |A' + B_1'\cos(2\psi) + C\cos(4\psi)|^2, \quad \text{(B5)}$$

where $A, A', B_1, B_1', B_2, B_2', C$, and C' are independent free parameters. Compared to Eqs. (B3), the presence of twofold symmetric terms, $\cos(2\psi)$ and $\sin(2\psi)$, breaks C_4 rotation symmetry while maintaining the mirror symmetries.

In the $4/m$ point group, the bulk electric dipole induced THG tensor is

$$
\chi_{ijkl}^{\mathrm{ED}} =
\begin{pmatrix}
\begin{pmatrix} xxxx & xxxy & 0 \\ xxxy & xxyy & 0 \\ 0 & 0 & xxzz \end{pmatrix} &
\begin{pmatrix} xxxy & xxyy & 0 \\ xxyy & xyyy & 0 \\ 0 & 0 & xyzz \end{pmatrix} &
\begin{pmatrix} 0 & 0 & xxzz \\ 0 & 0 & xyzz \\ xxzz & xyzz & 0 \end{pmatrix} \\
\begin{pmatrix} -xyyy & xxyy & 0 \\ xxyy & -xxxy & 0 \\ 0 & 0 & -xyzz \end{pmatrix} &
\begin{pmatrix} xxyy & -xxxy & 0 \\ -xxxy & xxxx & 0 \\ 0 & 0 & xxzz \end{pmatrix} &
\begin{pmatrix} 0 & 0 & -xyzz \\ 0 & 0 & xxzz \\ -xyzz & xxzz & 0 \end{pmatrix} \\
\begin{pmatrix} 0 & 0 & zxxz \\ 0 & 0 & 0 \\ zxxz & 0 & 0 \end{pmatrix} &
\begin{pmatrix} 0 & 0 & 0 \\ 0 & 0 & zxxz \\ 0 & zxxz & 0 \end{pmatrix} &
\begin{pmatrix} zxxz & 0 & 0 \\ 0 & zxxz & 0 \\ 0 & 0 & zzzz \end{pmatrix}
\end{pmatrix},
\tag{B6}
$$

leading to the azimuth-angle dependence of THG intensity as

$$I^{SS}(3\omega) \propto |A + B\cos(4\psi + \delta)|^2,$$

$$I^{PS}(3\omega) \propto |A' + B\sin(4\psi + \delta)|^2,$$

$$I^{SP}(3\omega) \propto |A + B\sin(4\psi + \delta)|^2,$$

$$I^{PP}(3\omega) \propto |A'' + B\cos(4\psi + \delta)|^2, \tag{B7}$$

where A, A', A'', B, and δ are adjustable parameters. Due to the δ offset, the THG patterns are rotated away from the principle axes and thus are not symmetric under reflections flipping either the a or b axis. The loss of mirror symmetries is also manifest in *PS* and *SP* geometries, where isotropic A and A' terms are added to the eightfold symmetric term $\sin(4\psi)^2$, leading to modulation of the lobe amplitudes and thus give

different intensities between the lobes at mirrored positions. Goodness of fits to the different point group tensors will be discussed in Appendix C.

APPENDIX C: RA-THG FITS TO LOW SYMMETRY POINT GROUPS

Following the scheme introduced in Ref. [37], the RA-THG signals are collected by a 2D electron-multiplying charge coupled device detector, which visualizes the azimuth dependence as the circular images shown in Figs. 10(a)–10(d). The CCD images are converted to the polar plots, whose quality of fits to different point group tensors can indicate structural distortions in the superlattice.
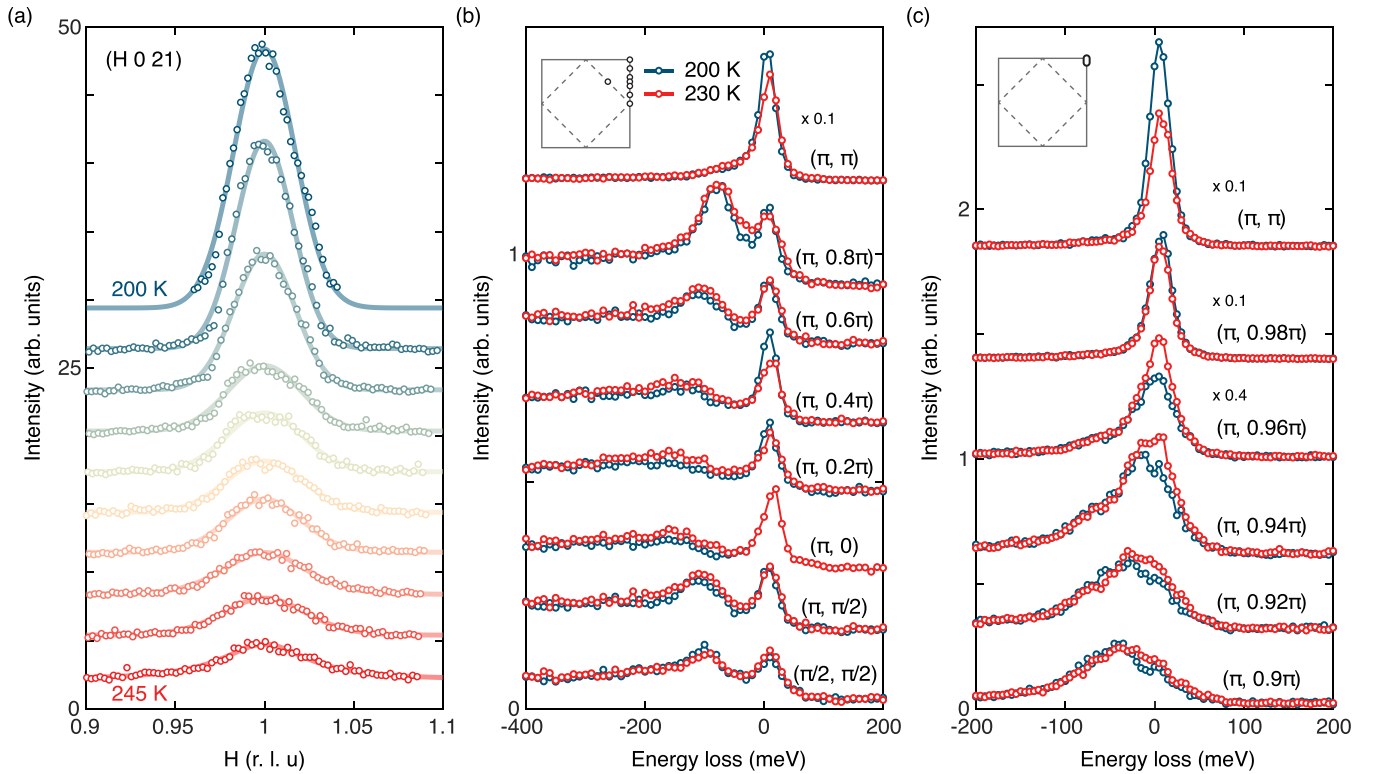
FIG. 11. Short range AFM order in SL above $T_N^A = 220$ K. (a) Temperature dependence of (H 0 21) scan, where double-layer contribution nearly vanishes. Each scan is acquired at every 5 K upon heating. (b) RIXS spectra below (blue) and above (red) T_N^A. (c) High resolution RIXS spectra near (π, π) magnetic zone center. Inset: Measured **q** points are marked by circles and enclosed in an ellipse in panels (b) and (c), respectively.

TABLE I. Irreducible representations and basis vectors for the magnetic structures allowed in the superlattice. m_i ($i = 1, \cdots, 6$) are independent parameters for the magnetic moments. As shown in Fig. 12(b), Iridium ions are located at a1:(0,0,0), a2:(1/2,1/2,0), b1:(0,1/2,δ), b2:(0,1/2,1-δ), b3:(1/2,0,δ), b4:(1/2,0,1-δ) of the unit cell Fig. 1(c), where $\delta = 0.3791$. The magnetic structure in Fig. 4(a) comprises canted ab-plane AFM of Γ_1 and c-axis collinear AFM of Γ_5.

Irreducible	Single layer		Double layer			
representation	a1	a2	b1	b2	b3	b4
Γ_1	$(m_1, m_2, 0)$ $(-m_2, m_1, 0)$	$(-m_1, m_2, 0)$ $(-m_2, -m_1, 0)$	$(m_3, m_4, 0)$ $(-m_6, -m_5, 0)$	$(m_5, m_6, 0)$ $(-m_4, -m_3, 0)$	$(-m_3, m_4, 0)$ $(-m_6, m_5, 0)$	$(-m_5, m_6, 0)$ $(-m_4, m_3, 0)$
Γ_2			$(0, 0, m_1)$	$(0, 0, -m_1)$	$(0, 0, m_1)$	$(0, 0, -m_1)$
Γ_3			$(0, 0, m_1)$	$(0, 0, m_1)$	$(0, 0, m_1)$	$(0, 0, -m_1)$
Γ_4	$(0, 0, m_1)$	$(0, 0, m_1)$	$(0, 0, m_2)$	$(0, 0, m_2)$	$(0, 0, m_2)$	$(0, 0, m_2)$
Γ_5	$(0, 0, m_1)$	$(0, 0, -m_1)$	$(0, 0, -m_2)$	$(0, 0, m_2)$	$(0, 0, m_2)$	$(0, 0, -m_2)$

In previous reports on Sr$_2$IrO$_4$ and Sr$_3$Ir$_2$O$_7$ [27,28], loss of mirror symmetries is evident from the azimuth profiles: the lobes are rotated away from high symmetry directions ($\sim 15°$ from the a axis) and/or show modulations with 8π periodicity such that the patterns are not symmetric with respect to the reflections flipping a or b axes. By contrast, in Fig. 3, the superlattice preserves the mirror symmetries.

To confirm, the polar plots are overlaid with the best fits to bulk electric dipole induced THG tensors for the 4/mmm point group as well as those for low symmetry mmm and 4/m point groups. Lowering the symmetry 4/mmm and allowing more adjustable parameters does not enhance the fit quality (see Fig. 10). R^2 values are 0.9379, 0.9514, and 0.9403 for 4/mmm, mmm, and 4/m point groups, respectively.

APPENDIX D: MAGNETIC CORRELATIONS IN THE SINGLE LAYER ABOVE T_N^A

It is rather unusual that the magnetic ordering in DL occurs across SL that remains paramagnetic down to T_N^A in the temperature range between $T_N^A = 220$ K and $T_N^B = 280$ K. Here, we verify that SL remains disordered and has no other long-range order above T_N^A. Figure 11(a) plots H scans upon heating across T_N^A at L = 21, where the SL contribution is selectively measured as the DL contribution is suppressed due to its structure factor [see Fig. 5(b)]. The magnetic reflection disappears above T_N^A, but short-range AFM magnetic correlations remain as a broad feature centered at (1 0).

To further confirm the short range (π, π) correlations in SL, we compare RIXS spectra below (blue) and above (red) T_N^A along high symmetry directions in Figs. 11(b) and 11(c).
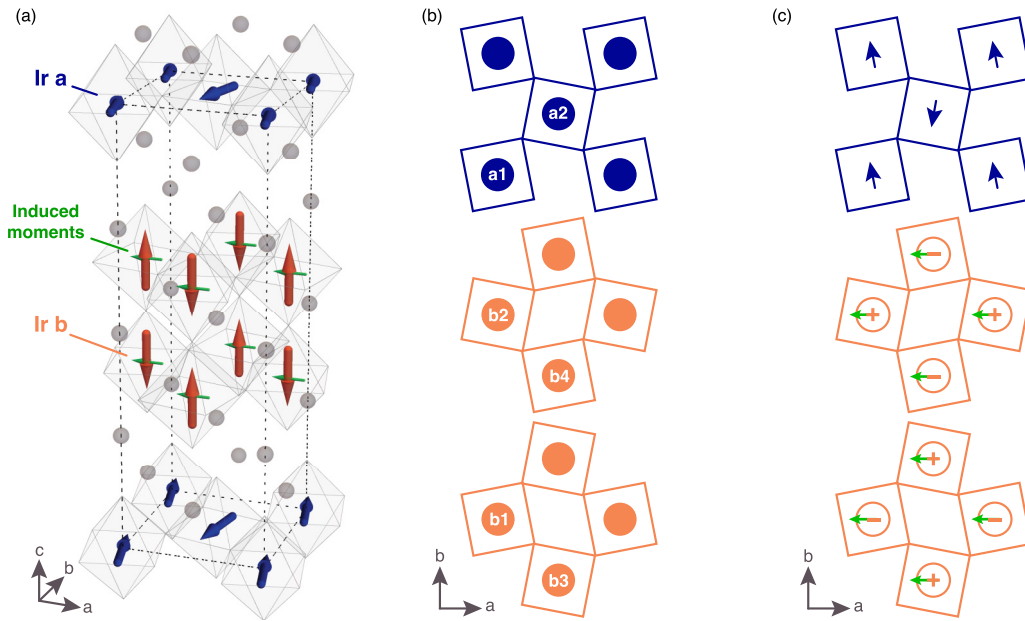

FIG. 12. (a) Superlattice magnetic structure with induced magnetic moments (green) based on the representation analysis. The net ferromagnetic moments in single layers (navy) can incline the c-axis AFM in double layers (orange), giving rise to small net in-plane moments in them (green). Grey spheres are Sr ions, and oxygens are indicated by octahedral cages. (b) The Wyckoff positions of the iridium ions in the single-layer (navy) and double-layer (orange) viewed from above. (c) The induced magnetic structure viewed from above. Plus (or minus) symbols in the double-layer indicate c-axis moments pointing upward (or downward).

For all measured **q** points, no significant change in spectra is found upon the magnetic ordering, except in the vicinity of the magnetic zone center. The high-resolution spectra in Fig. 11(c) also support that the loss of long-range magnetic order affects only long-wavelength magnons near (π, π). This indicates that no dramatic change occurs in SL apart from the diverging AFM correlation length, which rules out a transition to a different magnetic order at T_N^A.

APPENDIX E: REPRESENTATION ANALYSIS OF THE MAGNETIC STRUCTURE

We present a representation analysis based on the lattice structure shown in Fig. 1(c), assuming a **q** = 0 propagation vector based on the fact that all observed magnetic reflections have integer Miller indices. Its space group is $P\bar{4}b2$, which lacks inversion symmetry, and thus its point group ($\bar{4}m2$) is of lower symmetry than $4/mmm$. RA-THG is, however, insensitive to the inversion symmetry and has the same tensor structure for the two point groups. The inversion symmetry is broken by the way in which octahedra are rotated in DL in the current model. An inversion symmetric structure model can be made by doubling the unit cell in such a way that the octahedral rotation is opposite on two neighboring DLs. Thus, the determination of the presence of inversion symmetry requires full structure refinement, including the octahedral rotation on each layers, which is beyond the scope of this paper. However, our result that the magnetic orders in SL and DL belong to different irreducible representations (IR) is not affected by these details.

In the superlattice, iridium ions in SL and DL are not symmetry related and thus their magnetic structures are analyzed separately. The result of the analysis is shown in Table I. In both SL and DL, the *ab*-plane and *c*-axis components belong to different irreducible representations. This result can easily be seen from the transformation property under the twofold rotation about the *c* axis; the *ab*-plane moments are flipped, whereas the *c*-axis moments remain invariant. As long as the *ab*-plane and *c*-axis components are not mixed by any of the symmetry operations contained in the space group, their different characters for the twofold rotation guarantee that they belong to different IRs. Specifically, the canted *ab*-plane AFM of SL can be expressed by Γ_1 with $m_1, m_2 \neq 0$, while the *c*-axis collinear AFM of DL corresponds to Γ_5 with $m_2 \neq 0$.

Below $T_N^A = 220$ K, where the two symmetry-distinct orders coexist, it is in principle possible that interlayer interactions induce *ab*-plane (*c*-axis) moments in DL (SL). For example, in-plane ferromagnetic Γ_1 order of $m_4 = m_6 \neq 0$ can be induced in DL [see Figs. 12(a) and 12(c)], stabilized by the net ferromagnetic canted moments in the SL. However, such induced moments are expected to be very small due to the weak interlayer interactions compared to the strong Ising anisotropy and were not resolved in our RXD study.

[1] P. W. Anderson, The resonating valence bond state in La$_2$CuO$_4$ and superconductivity, Science **235**, 1196 (1987).

[2] P. A. Lee, N. Nagaosa, and X.-G. Wen, Doping a Mott insulator: Physics of high-temperature superconductivity, Rev. Mod. Phys. **78**, 17 (2006).

[3] B. Keimer, S. A. Kivelson, M. R. Norman, S. Uchida, and J. Zaanen, From quantum matter to high-temperature superconductivity in copper oxides, Nature (London) **518**, 179 (2015).

[4] N. Plakida, *High-Temperature Cuprate Superconductors* (Springer, Berlin, Heidelberg, 2010).

[5] A. Orendáčová, R. Tarasenko, V. Tkáč, E. Čižmár, M. Orendáč, and A. Feher, Interplay of spin and spatial anisotropy in low-dimensional quantum magnets with spin 1/2, Crystals **9**, 6 (2019).

[6] J. Bertinshaw, Y. K. Kim, G. Khaliullin, and B. J. Kim, Square lattice iridates, Annu. Rev. Condens. Matter Phys. **10**, 315 (2019).

[7] B. J. Kim, H. Jin, S. J. Moon, J.-Y. Kim, B.-G. Park, C. S. Leem, J. Yu, T. W. Noh, C. Kim, S.-J. Oh, J.-H. Park, V. Durairaj, G. Cao, and E. Rotenberg, Novel $J_{\text{eff}} = 1/2$ Mott State Induced by Relativistic Spin-Orbit Coupling in Sr$_2$IrO$_4$, Phys. Rev. Lett. **101**, 076402 (2008).

[8] G. Jackeli and G. Khaliullin, Mott Insulators in the Strong Spin-Orbit Coupling Limit: From Heisenberg to a Quantum Compass and Kitaev Models, Phys. Rev. Lett. **102**, 017205 (2009).

[9] B. J. Kim, H. Ohsumi, T. Komesu, S. Sakai, T. Morita, H. Takagi, and T. Arima, Phase-sensitive observation of a spin-orbital Mott state in Sr$_2$IrO$_4$, Science **323**, 1329 (2009).

[10] F. Wang and T. Senthil, Twisted Hubbard Model for Sr$_2$IrO$_4$: Magnetism and Possible High Temperature Superconductivity, Phys. Rev. Lett. **106**, 136402 (2011).

[11] Y. K. Kim, O. Krupin, J. D. Denlinger, A. Bostwick, E. Rotenberg, Q. Zhao, J. F. Mitchell, J. W. Allen, and B. J. Kim, Fermi arcs in a doped pseudospin-1/2 Heisenberg antiferromagnet, Science **345**, 187 (2014).

[12] Y. J. Yan, M. Q. Ren, H. C. Xu, B. P. Xie, R. Tao, H. Y. Choi, N. Lee, Y. J. Choi, T. Zhang, and D. L. Feng, Electron-Doped Sr$_2$IrO$_4$: An Analogue of Hole-Doped Cuprate Superconductors Demonstrated by Scanning Tunneling Microscopy, Phys. Rev. X **5**, 041018 (2015).

[13] Y. Cao, Q. Wang, J. A. Waugh, T. J. Reber, H. Li, X. Zhou, S. Parham, S. R. Park, N. C. Plumb, E. Rotenberg, A. Bostwick, J. D. Denlinger, T. Qi, M. A. Hermele, G. Cao, and D. S. Dessau, Hallmarks of the Mott-metal crossover in the hole-doped pseudospin-1/2 Mott insulator Sr$_2$IrO$_4$, Nat. Commun. **7**, 11367 (2016).

[14] Y. K. Kim, N. H. Sung, J. D. Denlinger, and B. J. Kim, Observation of a *d*-wave gap in electron-doped Sr$_2$IrO$_4$, Nat. Phys. **12**, 37 (2016).

[15] S. Sumita, T. Nomoto, and Y. Yanase, Multipole Superconductivity in Nonsymmorphic Sr$_2$IrO$_4$, Phys. Rev. Lett. **119**, 027001 (2017).

[16] J. Kim, D. Casa, M. H. Upton, T. Gog, Y.-J. Kim, J. F. Mitchell, M. van Veenendaal, M. Daghofer, J. van den Brink, G. Khaliullin, and B. J. Kim, Magnetic Excitation Spectra of Sr$_2$IrO$_4$ Probed by Resonant Inelastic X-Ray Scattering:

Establishing Links to Cuprate Superconductors, Phys. Rev. Lett. **108**, 177003 (2012).

[17] S. Fujiyama, H. Ohsumi, T. Komesu, J. Matsuno, B. J. Kim, M. Takata, T. Arima, and H. Takagi, Two-Dimensional Heisenberg Behavior of $J_{eff} = 1/2$ Isospins in the Paramagnetic State of the Spin-Orbital Mott Insulator Sr$_2$IrO$_4$, Phys. Rev. Lett. **108**, 247212 (2012).

[18] J. Jeong, Y. Sidis, A. Louat, V. Brouet, and P. Bourges, Time-reversal symmetry breaking hidden order in Sr$_2$(Ir, Rh)O$_4$, Nat. Commun. **8**, 15119 (2017).

[19] H. Murayama, K. Ishida, R. Kurihara, T. Ono, Y. Sato, Y. Kasahara, H. Watanabe, Y. Yanase, G. Cao, Y. Mizukami, T. Shibauchi, Y. Matsuda, and S. Kasahara, Bond Directional Anapole Order in a Spin-Orbit Coupled Mott Insulator Sr$_2$(Ir$_{1-x}$Rh$_x$)O$_4$, Phys. Rev. X **11**, 011021 (2021).

[20] L. Zhao, D. H. Torchinsky, H. Chu, V. Ivanov, R. Lifshitz, R. Flint, T. Qi, G. Cao, and D. Hsieh, Evidence of an odd-parity hidden order in a spin-orbit coupled correlated iridate, Nat. Phys. **12**, 32 (2016).

[21] K. L. Seyler, A. de la Torre, Z. Porter, E. Zoghlin, R. Polski, M. Nguyen, S. Nadj-Perge, S. D. Wilson, and D. Hsieh, Spin-orbit-enhanced magnetic surface second-harmonic generation in Sr$_2$IrO$_4$, Phys. Rev. B **102**, 201113(R) (2020).

[22] X. Chen, J. L. Schmehr, Z. Islam, Z. Porter, E. Zoghlin, K. Finkelstein, J. P. C. Ruff, and S. D. Wilson, Unidirectional spin density wave state in metallic (Sr$_{1-x}$La$_x$)$_2$IrO$_4$, Nat. Commun. **9**, 103 (2018).

[23] H. Liu and G. Khaliullin, Pseudo-Jahn-Teller Effect and Magnetoelastic Coupling in Spin-Orbit Mott Insulators, Phys. Rev. Lett. **122**, 057203 (2019).

[24] J. Porras, J. Bertinshaw, H. Liu, G. Khaliullin, N. H. Sung, J.-W. Kim, S. Francoual, P. Steffens, G. Deng, M. M. Sala, A. Efimenko, A. Said, D. Casa, X. Huang, T. Gog, J. Kim, B. Keimer, and B. J. Kim, Pseudospin-lattice coupling in the spin-orbit Mott insulator Sr$_2$IrO$_4$, Phys. Rev. B **99**, 085125 (2019).

[25] L. L. Hu, M. Yang, Y. L. Wu, Q. Wu, H. Zhao, F. Sun, W. Wang, R. He, S. L. He, H. Zhang, R. J. Huang, L. F. Li, Y. G. Shi, and J. Zhao, Strong pseudospin-lattice coupling in Sr$_3$Ir$_2$O$_7$: Coherent phonon anomaly and negative thermal expansion, Phys. Rev. B **99**, 094307 (2019).

[26] F. Ye, S. Chi, B. C. Chakoumakos, J. A. Fernandez-Baca, T. Qi, and G. Cao, Magnetic and crystal structures of Sr$_2$IrO$_4$: A neutron diffraction study, Phys. Rev. B **87**, 140406(R) (2013).

[27] D. H. Torchinsky, H. Chu, L. Zhao, N. B. Perkins, Y. Sizyuk, T. Qi, G. Cao, and D. Hsieh, Structural Distortion-Induced Magnetoelastic Locking in Sr$_2$IrO$_4$ Revealed Through Nonlinear Optical Harmonic Generation, Phys. Rev. Lett. **114**, 096404 (2015).

[28] T. Hogan, L. Bjaalie, L. Zhao, C. Belvin, X. Wang, C. G. Van de Walle, D. Hsieh, and S. D. Wilson, Structural investigation of the bilayer iridate Sr$_3$Ir$_2$O$_7$, Phys. Rev. B **93**, 134110 (2016).

[29] S. Boseggia, H. C. Walker, J. Vale, R. Springell, Z. Feng, R. S. Perry, M. M. Sala, H. M. Rønnow, S. P. Collins, and D. F. McMorrow, Locking of iridium magnetic moments to the correlated rotation of oxygen octahedra in Sr$_2$IrO$_4$ revealed by x-ray resonant scattering, J. Phys.: Condens. Matter **25**, 422202 (2013).

[30] G. Cao, Y. Xin, C. S. Alexander, J. E. Crow, P. Schlottmann, M. K. Crawford, R. L. Harlow, and W. Marshall, Anomalous magnetic and transport behavior in the magnetic insulator Sr$_3$Ir$_2$O$_7$, Phys. Rev. B **66**, 214412 (2002).

[31] I. Nagai, Y. Yoshida, S. I. Ikeda, H. Matsuhata, H. Kito, and M. Kosaka, Canted antiferromagnetic ground state in Sr$_3$Ir$_2$O$_7$, J. Phys.: Condens. Matter **19**, 136214 (2007).

[32] J. Chaloupka, G. Jackeli, and G. Khaliullin, Kitaev-Heisenberg Model on a Honeycomb Lattice: Possible Exotic Phases in Iridium Oxides A_2IrO$_3$, Phys. Rev. Lett. **105**, 027204 (2010).

[33] M. K. Crawford, M. A. Subramanian, R. L. Harlow, J. A. Fernandez-Baca, Z. R. Wang, and D. C. Johnston, Structural and magnetic studies of Sr$_2$IrO$_4$, Phys. Rev. B **49**, 9198 (1994).

[34] H. Matsuhata, I. Nagai, Y. Yoshida, S. Hara, S.-I. Ikeda, and N. Shirakawa, Crystal structure of Sr$_3$Ir$_2$O$_7$ investigated by transmission electron microscopy, J. Solid State Chem. **177**, 3776 (2004).

[35] R. L. Harlow, Z. G. Li, W. J. Marshall, M. K. Crawford, and M. A. Subramanian, Effects of stacking faults on refinement of single crystal X-ray diffraction data for Sr$_5$Ir$_3$O$_{11}$, Mater. Research Bull. **30**, 217 (1995).

[36] D. H. Torchinsky, H. Chu, T. Qi, G. Cao, and D. Hsieh, A low temperature nonlinear optical rotational anisotropy spectrometer for the determination of crystallographic and electronic symmetries, Rev. Sci. Instrum. **85**, 083102 (2014).

[37] J. W. Harter, L. Niu, A. J. Woss, and D. Hsieh, High-speed measurement of rotational anisotropy nonlinear optical harmonic generation using position-sensitive detection, Opt. Lett. **40**, 4671 (2015).

[38] J. E. Sipe, D. J. Moss, and H. M. van Driel, Phenomenological theory of optical second- and third-harmonic generation from cubic centrosymmetric crystals, Phys. Rev. B **35**, 1129 (1987).

[39] D. G. Mazzone, D. Meyers, Y. Cao, J. G. Vale, C. D. Dashwood, Y. Shi, A. J. A. James, N. J. Robinson, J. Lin, V. Thampy, Y. Tanaka, A. S. Johnson, H. Miao, R. Wang, T. A. Assefa, J. Kim, D. Casa, R. Mankowsky, D. Zhu, R. Alonso-Mori *et al.*, Laser-induced transient magnons in Sr$_3$Ir$_2$O$_7$ throughout the Brillouin zone, Proc. Natl. Acad. Sci. USA **118**, e2103696118 (2021).

[40] J. Kim, A. H. Said, D. Casa, M. H. Upton, T. Gog, M. Daghofer, G. Jackeli, J. van den Brink, G. Khaliullin, and B. J. Kim, Large Spin-Wave Energy Gap in the Bilayer Iridate Sr$_3$Ir$_2$O$_7$: Evidence for Enhanced Dipolar Interactions Near the Mott Metal-Insulator Transition, Phys. Rev. Lett. **109**, 157402 (2012).

[41] J. G. Vale, S. Boseggia, H. C. Walker, R. Springell, Z. Feng, E. C. Hunter, R. S. Perry, D. Prabhakaran, A. T. Boothroyd, S. P. Collins, H. M. Rønnow, and D. F. McMorrow, Importance of XY anisotropy in Sr$_2$IrO$_4$ revealed by magnetic critical scattering experiments, Phys. Rev. B **92**, 020406(R) (2015).

[42] V. Y. Irkhin and A. A. Katanin, Kosterlitz-Thouless and magnetic transition temperatures in layered magnets with a weak easy-plane anisotropy, Phys. Rev. B **60**, 2990 (1999).

[43] N. Suzuki and H. Kamimura, Theory of spin-dependent phonon Raman scattering in magnetic crystals, J. Phys. Soc. Jpn. **35**, 985 (1973).

[44] E. Granado, A. García, J. A. Sanjurjo, C. Rettori, I. Torriani, F. Prado, R. D. Sánchez, A. Caneiro, and S. B. Oseroff, Magnetic ordering effects in the Raman spectra of La$_{1-x}$Mn$_{1-x}$O$_3$, Phys. Rev. B **60**, 11879 (1999).

[45] H. J. Zeiger, J. Vidal, T. K. Cheng, E. P. Ippen, G. Dresselhaus, and M. S. Dresselhaus, Theory for displacive excitation of coherent phonons, Phys. Rev. B **45**, 768 (1992).